

Accessing the Longitudinally Polarized Photon Content of the Proton

A. Mukherjee* and C. Pisano†

Institut für Physik, Universität Dortmund, D 44221 Dortmund, Germany

(Dated: November 17, 2018)

Abstract

We investigate the QED Compton process (QEDCS) in longitudinally polarized lepton-proton scattering both in the elastic and inelastic channels and show that the cross section can be expressed in terms of the polarized equivalent photon distribution of the proton. We provide the necessary kinematical constraints to extract the polarized photon content of the proton using this process at HERMES, COMPASS and eRHIC. We also discuss the suppression of the major background process coming from virtual Compton scattering. We point out that such an experiment can give valuable information on $g_1(x_B, Q^2)$ in the small x_B , broad Q^2 region at the future polarized collider eRHIC and especially in the lower Q^2 , medium x_B region in fixed target experiments.

*Electronic address: asmita@physik.uni-dortmund.de

†Electronic address: pisano@harpo.physik.uni-dortmund.de

I. INTRODUCTION

QED Compton process (QEDCS) in the scattering $lp \rightarrow l\gamma X$, where l is a lepton, has a distinctive experimental signature: both the outgoing lepton and photon are detected at large polar angles and almost back to back in azimuth, such that their transverse momenta almost balance each other, with little or no hadronic activity at the detector [1, 2]. In fact, such a reaction in the unpolarized $e - p$ scattering has long been suggested as an excellent channel not only to determine the structure function $F_2(x_B, Q^2)$ of the proton but also to extract the equivalent photon content of the proton [1, 2, 3]. In a recent Monte Carlo analysis of the QED Compton process performed by some members of the H1 collaboration at HERA [4], it was found that, although the cross section in the elastic channel was accurately described by the equivalent photon approximation (EPA), this was not the case in the inelastic channel. In two previous papers [5, 6] we have suggested improved kinematical cuts for a more accurate extraction of the unpolarized equivalent photon distribution of the proton which furthermore suppress the major background process coming from virtual Compton scattering (VCS). In this work we study the QED Compton process in the polarized scattering $\vec{l}\vec{p} \rightarrow l\gamma X$ (both elastic and inelastic channels), where the initial lepton and proton are longitudinally polarized. We show that when the virtuality of the exchanged photon is not too large, the cross section can be approximated as a convolution of the longitudinally polarized equivalent photon distribution of the proton [7, 8] and the real photoproduction cross section. We provide the necessary kinematical constraints to extract the polarized photon content of the proton at HERMES, COMPASS and eRHIC (the future polarized ep collider planned at BNL). In addition, we show that such an experiment can also access the polarized structure function $g_1(x_B, Q^2)$ at HERMES in the low Q^2 region and at eRHIC over a wide range of the Bjorken scaling variable x_B and Q^2 . $g_1(x_B, Q^2)$ and its first x_B moment in the low Q^2 region have been studied in fully inclusive measurements at SLAC [9], HERMES [10, 11] and JLab [12, 13]. The most recent measurements by CLAS [14] are in the kinematical region $Q^2 = 0.15 - 1.64$ GeV 2 . The low Q^2 region is of particular interest because contributions due to nonperturbative dynamics dominate here and thus the transition from soft to hard physics can be studied. In fact the data in [14] clearly indicate a dominant contribution from the resonances and at higher Q^2 it is below the perturbative QCD evolved scaling value of g_1 . This in fact illustrates the necessity of further

investigation of $g_1(x_B, Q^2)$ in the transition region. In these fixed target experiments, low Q^2 is associated with low values of x_B , thus the covered kinematical region is smaller compared to the unpolarized data. Data on $g_1(x_B, Q^2)$ for small x_B and in the scaling region are missing due to the absence of polarized colliders so far (with the exception of RHIC, which has started operating in the polarized mode for pp collisions only very recently). The small x_B region is again interesting; it is the region of high parton densities, and measurements in this region will provide information about the effects of large $(\alpha_s \ln^2 \frac{1}{x_B})^k$ resummation and DGLAP evolution, and also about the 'soft' to 'hard' scale transition [15, 16, 17]. A better understanding of $g_1(x_B, Q^2)$ in this region is necessary in order to determine its first moment experimentally. The kinematics of QED Compton events is different from the one of inclusive deep inelastic scattering due to the radiated photon in the final state and thus it provides a novel way to access $g_1(x_B, Q^2)$ in a kinematical region not well covered by inclusive measurements (also for $F_2(x_B, Q^2)$ [4]).

The plan of the paper is as follows. In section II and III, we derive the analytic expressions of the cross section for the polarized QED Compton process in the elastic and inelastic channel, respectively. In section IV, we discuss the background coming from virtual Compton scattering (VCS) and also the interference between QEDCS and VCS. The numerical results are presented in section V. Summary and conclusions are given in section VI. The analytic expressions of the matrix elements are given in Appendices A and B.

II. ELASTIC QED COMPTON SCATTERING

We consider QED Compton scattering in the elastic process:

$$\vec{e}(l) + \vec{p}(P) \rightarrow e(l') + \gamma(k') + p(P'), \quad (2.1)$$

where the incident electron and proton are longitudinally polarized and the 4-momenta of the particles are given in brackets. Instead of the electron, one can also consider a muon beam (COMPASS); the analytic expressions will be the same. We introduce the invariants

$$S = (P + l)^2, \quad \hat{s} = (l + k)^2, \quad t = k^2. \quad (2.2)$$

$k = P - P'$ is the 4-momentum of the virtual photon. The photon in the final state is real, $k'^2 = 0$. We neglect the electron mass everywhere except when it is necessary to avoid

divergences in the formulae and take the proton to be massive, $P^2 = P'^2 = m^2$. The relevant Feynman diagrams for this process are shown in Fig. 1, with X being a proton and $P_X = P'$. The squared matrix element can be written as

$$|\Delta M_{\text{el}}^{QEDCS}|^2 = \frac{1}{t^2} H_{\text{el}}^{A\mu\nu}(P, P') T_{\mu\nu}^A(l, k; l', k'), \quad (2.3)$$

$H_{\text{el}}^{A\mu\nu}(P, P')$ and $T_{\mu\nu}^A(l, k; l', k')$ being the antisymmetric parts of the hadronic tensor and leptonic tensor respectively, which contribute to the polarized cross section. As before [5], we use the notation

$$dPS_N(P; P_1, \dots, P_N) = (2\pi)^4 \delta\left(P - \sum_{i=1}^N P_i\right) \prod_{i=1}^N \frac{d^3 P_i}{(2\pi)^3 2P_i^0} \quad (2.4)$$

for the Lorentz invariant N -particle phase-space element. The cross section can be written as

$$\Delta\sigma_{\text{el}}(S) = \frac{1}{2(S - m^2)} \int dPS_{2+1}(l + P; l', k', P') |\Delta M_{\text{el}}^{QEDCS}|^2. \quad (2.5)$$

Following the same approach as in [5, 18] we can write this as

$$\Delta\sigma_{\text{el}}(S) = \frac{1}{2(S - m^2)} \int \frac{d\hat{s}}{2\pi} dPS_2(l + P; l' + k', P') \frac{1}{t^2} H_{\text{el}}^{A\mu\nu}(P, P') X_{\mu\nu}^A(l, k). \quad (2.6)$$

$X_{\mu\nu}^A$ contains all the informations about the leptonic part of the process and is defined as

$$X_{\mu\nu}^A(l, k) = \int dPS_2(l + k; l', k') T_{\mu\nu}^A(l, k; l', k'), \quad (2.7)$$

$T_{\mu\nu}^A(l, k; l', k')$ is the antisymmetric part of the leptonic tensor,

$$T_A^{\mu\nu}(l, k; l', k') = -\frac{4ie^4}{\hat{s}\hat{u}} \epsilon^{\mu\nu\alpha\beta} k_\beta \left[(\hat{s} - t)l_\alpha + (\hat{u} - t)l'_\alpha \right]. \quad (2.8)$$

Here $e^2 = 4\pi\alpha$ and we have defined $\hat{t} = (l - l')^2$ and $\hat{u} = (l - k')^2$.

For polarized scattering, $X_{\mu\nu}^A$ is antisymmetric in the indices μ, ν and can be expressed in terms of the Lorentz scalar \tilde{X}_2^A :

$$X_A^{\mu\nu} = -\frac{i}{(\hat{s} - t)} \epsilon^{\mu\nu\alpha\beta} k_\alpha l_\beta \tilde{X}_2^A(\hat{s}, t), \quad (2.9)$$

with

$$\tilde{X}_2^A(\hat{s}, t) = -2X_{\mu\nu}^A P_A^{\mu\nu}. \quad (2.10)$$

$P_A^{\mu\nu}$ is the antisymmetric part of the photon polarization density matrix [19]:

$$P_A^{\mu\nu} = \frac{1}{2}(\epsilon^\mu \epsilon^{\nu*} - \epsilon^\nu \epsilon^{\mu*}) = \frac{i}{2\sqrt{|k^2|}} \epsilon^{\mu\nu\rho\sigma} k_\rho t_\sigma \quad (2.11)$$

where t_σ is the spin vector of the photon:

$$t_\sigma = N_t \left(k_\sigma - \frac{k^2}{l \cdot k} l_\sigma \right); \quad N_t = \frac{1}{\sqrt{|k^2|}}. \quad (2.12)$$

We define the functions $X_2^A(\hat{s}, t, \hat{t})$ as

$$\tilde{X}_2^A(\hat{s}, t) = 2\pi \int_{\hat{t}_{\min}}^{\hat{t}_{\max}} d\hat{t} X_2^A(\hat{s}, t, \hat{t}). \quad (2.13)$$

The integration limits are given by Eq. (2.18) of [5]. $X_2^A(\hat{s}, t, \hat{t})$ can be obtained using the leptonic tensor given above:

$$X_2^A(\hat{s}, t, \hat{t}) = \frac{4\alpha^2}{\hat{s}\hat{u}(\hat{s}-t)} \left[(\hat{s}-t)^2 + \frac{2\hat{t}(\hat{u}-t)}{\hat{s}-t} - (\hat{s}+\hat{t})^2 \right]. \quad (2.14)$$

The hadronic tensor for polarized scattering is expressed in terms of the proton form factors as [7, 20],

$$H_{\mu\nu}^A = -ie^2 \epsilon^{\mu\nu\rho\sigma} m k_\rho \left[2G_E G_M S_\sigma - \frac{G_M(G_M - G_E)}{1+\tau} \frac{k \cdot S}{m^2} P_\sigma \right], \quad (2.15)$$

with $\tau = \frac{-t}{4m^2}$ and $S_\sigma = \frac{1}{m}(P_\sigma - \frac{m^2}{P \cdot l} l_\sigma)$ being the spin vector of the proton which satisfies $S^2 = -1$ and $P \cdot S = 0$. G_E and G_M are the proton electric and magnetic form factors and are empirically parametrized as dipoles:

$$G_E(t) = \frac{1}{[1 - t/(0.71 \text{ GeV}^2)]^2}, \quad G_M(t) = 2.79 G_E(t). \quad (2.16)$$

The elastic cross section can then be written as

$$\begin{aligned} \Delta\sigma_{\text{el}} = & \frac{\alpha}{8\pi(S-m^2)^2} \int_{m_e^2}^{(\sqrt{S}-m)^2} d\hat{s} \int_{t_{\min}}^{t_{\max}} \frac{dt}{t} \int_{\hat{t}_{\min}}^{\hat{t}_{\max}} d\hat{t} \int_0^{2\pi} d\phi X_2^A(\hat{s}, t, \hat{t}) \\ & \left[\left(2 \frac{S-m^2}{\hat{s}-t} - 1 + \frac{2m^2}{t} \frac{\hat{s}-t}{S-m^2} \right) G_M^2(t) \right. \\ & \left. - 2 \left(\frac{S-m^2}{\hat{s}-t} - 1 + \frac{m^2}{t} \frac{\hat{s}-t}{S-m^2} \right) \frac{G_M(G_M - G_E)}{1+\tau} \right]. \end{aligned} \quad (2.17)$$

ϕ is the azimuthal angle of the outgoing $e - \gamma$ system in the center of momentum frame. The limits of integration are the same as in Eqs. (2.18) and (2.24) of [5]. These limits are

modified due to the experimental cuts which we impose numerically. In the EPA limit, we neglect $|t|$ vs. \hat{s} and m^2 vs. S and get

$$X_2^A(\hat{s}, t, \hat{t}) \approx X_2^A(\hat{s}, 0, \hat{t}) = \frac{4\alpha^2}{\hat{s}} \left(\frac{\hat{s}}{\hat{u}} - \frac{\hat{u}}{\hat{s}} \right) = -\frac{2\hat{s}}{\pi} \frac{d\Delta\hat{\sigma}^{e\gamma \rightarrow e\gamma}}{d\hat{t}}, \quad (2.18)$$

where $\frac{d\hat{\sigma}}{d\hat{t}}$ is the differential real photoproduction cross section and $\tilde{X}_2^A(\hat{s}, 0) = -4\hat{s}\Delta\hat{\sigma}$. The elastic cross section then becomes

$$\Delta\sigma_{\text{el}} \approx \Delta\sigma_{\text{el}}^{\text{EPA}} = \int_{x_{\min}}^{(1-\frac{m}{\sqrt{S}})^2} dx \int_{m_e^2 - \hat{s}}^0 d\hat{t} \Delta\gamma_{\text{el}}(x) \frac{d\Delta\hat{\sigma}(xS, \hat{t})}{d\hat{t}} \quad (2.19)$$

where m_e is the mass of the electron and $\Delta\gamma_{\text{el}}(x)$ is the elastic contribution to the polarized equivalent photon distribution of the proton [7]

$$\Delta\gamma_{\text{el}}(x) = -\frac{\alpha}{2\pi} \int_{t_{\min}}^{t_{\max}} \frac{dt}{t} \left[\left(2 - x + \frac{2m^2 x^2}{t} \right) G_M^2 - 2 \left(1 - x + \frac{m^2 x^2}{t} \right) \frac{G_M(G_M - G_E)}{1 + \tau} \right] \quad (2.20)$$

with $x = \frac{\hat{s}}{S}$ and the limits of integration are given by Eq. (2.30) of [5].

III. INELASTIC QED COMPTON SCATTERING

We next consider the corresponding inelastic process

$$\vec{e}(l) + \vec{p}(P) \rightarrow e(l') + \gamma(k') + X(P_X), \quad (3.1)$$

where $P_X = \sum_{X_i} P_{X_i}$ is the sum over all momenta of the produced hadronic system. We take the invariant mass of the produced hadronic system to be W . The Bjorken variable x_B is defined as

$$x_B = \frac{Q^2}{2P \cdot (-k)} = \frac{Q^2}{Q^2 + W^2 - m^2}, \quad (3.2)$$

where $Q^2 = -k^2 = -t$. The cross section for inelastic scattering reads:

$$\Delta\sigma_{\text{inel}}(S) = \frac{1}{16\pi^2(S - m^2)^2} \int_{W_{\min}^2}^{W_{\max}^2} dW^2 \int_{m_e^2}^{(\sqrt{S} - W)^2} d\hat{s} \int_{Q_{\min}^2}^{Q_{\max}^2} \frac{dQ^2}{Q^4} W_A^{\mu\nu} X_{\mu\nu}^A, \quad (3.3)$$

where $X_{\mu\nu}^A$ is given by Eq. (2.9) and $W_A^{\mu\nu}$ is the hadronic tensor:

$$W_A^{\mu\nu} = ie^2 \frac{m}{P \cdot k} \epsilon^{\mu\nu\rho\sigma} k_\rho \left[g_1(k^2, P \cdot k) S_\sigma + g_2(k^2, P \cdot k) \left(S_\sigma - \frac{k \cdot S}{k \cdot P} P_\sigma \right) \right] \quad (3.4)$$

with $S_\sigma = \frac{1}{m} \left(P_\sigma - \frac{m^2}{P \cdot l} l_\sigma \right)$ being the polarization of the proton, satisfying $S^2 = -1$ and $P \cdot S = 0$.

The cross section can be written as

$$\begin{aligned} \Delta\sigma_{\text{inel}}(S) &= \frac{\alpha}{4\pi(S-m^2)^2} \int_{W_{\text{min}}^2}^{W_{\text{max}}^2} dW^2 \int_{m_e^2}^{(\sqrt{S}-m)^2} d\hat{s} \int_{Q_{\text{min}}^2}^{Q_{\text{max}}^2} \frac{dQ^2}{Q^2} \frac{1}{(W^2+Q^2-m^2)} \\ &\times \left\{ \left[-2 \frac{S-m^2}{\hat{s}+Q^2} + \frac{W^2+Q^2-m^2}{Q^2} + \frac{2m^2}{Q^2} \left(\frac{\hat{s}+Q^2}{S-m^2} \right) \right] g_1(x_B, Q^2) \right. \\ &\left. + \frac{4m^2}{W^2+Q^2-m^2} g_2(x_B, Q^2) \right\} \tilde{X}_2^A(\hat{s}, Q^2), \end{aligned} \quad (3.5)$$

here $\tilde{X}_2^A(\hat{s}, Q^2) = 2\pi \int_{\hat{t}_{\text{min}}}^{\hat{t}_{\text{max}}} d\hat{t} X_2^A(\hat{s}, Q^2, \hat{t})$ with $X_2^A(\hat{s}, Q^2, \hat{t})$ given by Eq. (2.14). The limits of the Q^2 , W^2 and \hat{t} integrations are given in Eqs. (3.11), (3.12) and (2.18) of [5] respectively. In the limit of the EPA, as before, we approximate $S-m^2 \approx S$ and $\hat{s}+Q^2 \approx \hat{s}$; the cross section then becomes

$$\Delta\sigma_{\text{inel}}(S) \approx \Delta\sigma_{\text{inel}}^{\text{EPA}} = \int_{x_{\text{min}}}^{(1-m/\sqrt{S})^2} dx \int_{m_e^2-\hat{s}}^0 d\hat{t} \Delta\gamma_{\text{inel}}(x, xS) \frac{\Delta d\hat{\sigma}(xS, \hat{t})}{d\hat{t}}, \quad (3.6)$$

where again $x = \hat{s}/S$ and $\Delta\gamma_{\text{inel}}(x, xS)$ is the inelastic contribution to the polarized equivalent photon distribution of the proton:

$$\Delta\gamma_{\text{inel}}(x, xS) = \frac{\alpha}{2\pi} \int_x^1 \frac{dy}{y} \int_{Q_{\text{min}}^2}^{Q_{\text{max}}^2} \frac{dQ^2}{Q^2} \left(2 - y - \frac{2m^2 x^2}{Q^2} \right) 2g_1\left(\frac{x}{y}, Q^2\right), \quad (3.7)$$

where we have taken the scale to be \hat{s} . Here we have neglected the contribution from $g_2(x_B, Q^2)$. Expressing $g_1(x_B, Q^2)$ in terms of the polarized quark and antiquark distributions, one can confirm that the above expression reduces to that given in [7, 8]. However, in this case, one chooses the minimal (but not compelling) boundary condition $\Delta\gamma(x, Q_0^2) = 0$ at a scale $Q_0^2 = 0.26 \text{ GeV}^2$. Eq. (3.7) is free from this particular boundary condition. The limits of the Q^2 integration can be approximated similar to the unpolarized case (see Eq. (3.16) of [5]).

IV. BACKGROUND FROM VIRTUAL COMPTON SCATTERING

The cross section of the process in Eq. (3.1) (also the elastic channel) receives contribution from the virtual Compton Scattering (VCS), when the photon is emitted from the proton side (see Fig. 2) as well as the interference between the QED Compton scattering (QEDCS)

and VCS. The cross section for the elastic process is given by

$$\Delta\sigma_{\text{el}}(S) = \frac{\alpha^3}{8\pi(S-m^2)^2} \int_{m_e^2}^{(\sqrt{S}-m)^2} d\hat{s} \int_{t_{\min}}^{t_{\max}} dt \int_{\hat{t}_{\min}}^{\hat{t}_{\max}} d\hat{t} \int_0^{2\pi} d\phi \frac{1}{(\hat{s}-t)} |\Delta M_{\text{el}}|^2, \quad (4.1)$$

where

$$|\Delta M_{\text{el}}|^2 = |\Delta M_{\text{el}}^{\text{QEDCS}}|^2 + |\Delta M_{\text{el}}^{\text{VCS}}|^2 - 2 \Re e \Delta M_{\text{el}}^{\text{QEDCS}} \Delta M_{\text{el}}^{\text{VCS}*} \quad (4.2)$$

is the matrix element squared of the subprocess. The limits of integrations are the same as in Eq. (2.17). The interference term will have opposite sign if we consider a positron instead of an electron. The cross section of the VCS process is expressed in terms of generalized parton distributions and one needs a realistic model for a quantitative estimate of this background [21]. Here, in order to find the constraints to suppress the VCS, we make a simplified assumption: we take the proton to be a massive pointlike particle with an effective $\gamma^* p$ vertex, $-i\gamma^\mu F_1(t)$. The explicit expressions for the matrix elements are given in Appendix A.

Particularly interesting for our purpose of extracting the polarized photon distribution of the proton is the inelastic channel. Here we use a unified parton model (similar to our analysis in [6]) to estimate the VCS and QEDCS rates. The cross section within the parton model is given by

$$\frac{d\Delta\sigma_{\text{inel}}}{dx_B dQ^2 d\hat{s} d\hat{t} d\phi} = \sum_q \Delta q(x_B, Q^2) \frac{d\Delta\hat{\sigma}^q}{d\hat{s} dQ^2 d\hat{t} d\phi}, \quad (4.3)$$

where $\Delta q(x_B, Q^2)$ are the polarized quark and antiquark distributions of the initial proton, $q = u, d, s, \bar{u}, \bar{d}, \bar{s}$ and $d\Delta\hat{\sigma}^q$ is the differential cross section of the subprocess

$$\vec{e}(l) + \vec{q}(p) \rightarrow e(l') + \gamma(k') + q(p'). \quad (4.4)$$

Here \vec{q} is a longitudinally polarized quark in a longitudinally polarized proton and q is a quark in the final state. The integrated cross section becomes

$$\begin{aligned} \Delta\sigma_{\text{inel}}(S) = & \frac{\alpha^3}{8\pi(S-m^2)^2} \sum_q \int_{W_{\min}^2}^{W_{\max}^2} dW^2 \int_{m_e^2}^{(\sqrt{S}-W)^2} d\hat{s} \int_{Q_{\min}^2}^{Q_{\max}^2} \frac{dQ^2}{Q^2} \int_{\hat{t}_{\min}}^{\hat{t}_{\max}} d\hat{t} \int_0^{2\pi} d\phi \frac{1}{(\hat{s}+Q^2)} \\ & \times |\Delta M_{\text{inel}}|^2 \Delta q(x_B, Q^2), \end{aligned} \quad (4.5)$$

where

$$|\Delta M_{\text{inel}}|^2 = |\Delta M_{\text{inel}}^{\text{QEDCS}}|^2 + |\Delta M_{\text{inel}}^{\text{VCS}}|^2 - 2 \Re e \Delta M_{\text{inel}}^{\text{QEDCS}} \Delta M_{\text{inel}}^{\text{VCS}*}. \quad (4.6)$$

The limits of integrations are the same as in Eq. (17) of [6]. The explicit expression of the matrix element is given in the appendix B. It is useful to define the auxiliary invariants $\hat{S} = (p' + k')^2$ and $\hat{U} = (p' - k)^2$, which can be written in terms of measurable quantities,

$$\hat{S} = \frac{\hat{t}(x_l - x_B)}{x_l}, \quad \hat{U} = \hat{t} - \hat{S} + Q^2, \quad (4.7)$$

with $x_l = \frac{-\hat{t}}{2P \cdot (l - l')}$. In addition to the leptonic variable x_l we define $x_\gamma = \frac{l \cdot k}{P \cdot l}$, which represents the fraction of the longitudinal momentum of the proton carried by the virtual photon [5]. In the limit of the EPA, both x_l and x_γ are the same and become equal to x .

V. NUMERICAL RESULTS

In this section, we present our numerical results. The cuts used for HERMES, COMPASS and eRHIC kinematics are given in Table I. The constraints on the energies and polar angles of the detected particles reduce the background contributions coming from the radiative emissions (when the final state photon is emitted along the incident or the final lepton line), because they prevent the lepton propagators to become too small [1, 22]. QED Compton events are singled out at HERA by imposing a maximum limit on the acoplanarity angle ϕ_A which is defined as $\phi_A = |\pi - |\phi_\gamma - \phi_e||$, where ϕ_γ and ϕ_e are the azimuthal angles of the outgoing photon and electron, respectively. We have observed [5, 6] that instead of this limit on ϕ_A , the constraint $\hat{s} > Q^2$, which is applicable experimentally, is more efficient in extracting the equivalent photon distribution from the 'exact' result. Here we use this constraint.

The unpolarized cross sections have been calculated using the formulae in [5] but for HERMES, COMPASS and eRHIC kinematics, respectively. In the numerical estimate of the unpolarized cross section, we have used ALLM97 parametrization [23] of the structure function $F_2(x_B, Q^2)$ as before, which is obtained by fitting DIS data of HERA and fixed target experiments together with the total pp and γp cross sections measured and is expected to hold over the entire range of x_B and Q^2 . We have taken $F_L(x_B, Q^2)$ to be zero, assuming the Callan-Gross relation, similar to [4, 22]. In the polarized cross section, we have neglected the contribution from $g_2(x_B, Q^2)$ and used the parametrization of [24] for $g_1(x_B, Q^2)$. In this parametrization, $g_1(x_B, Q^2)$ is described in the low- Q^2 region by the GVMD model together with the Drell-Hearn-Gerasimov-Hosoda-Yamamoto sum rule and the asymptotic

part of $g_1(x_B, Q^2)$ is expressed in terms of NLO GRSV00 [25] parton distributions (standard scenario) in terms of a suitably defined scaling variable $\bar{x} = \frac{Q^2+Q_0^2}{Q^2+Q_0^2+W^2-M^2}$ with $Q_0^2 = 1.2$ GeV 2 . The scale Q^2 is changed to $Q^2 + Q_0^2$, so as to extrapolate to low- Q^2 region. It is to be noted that for QED Compton scattering, the effects of $F_L(x_B, Q^2)$ and $g_2(x_B, Q^2)$ have to be taken into account in a more accurate study as their effect may become non-negligible in the low- Q^2 region. However, this is beyond the scope of the present work.

Before discussing the results for specific experiments, it is interesting to investigate some general properties of the total cross section. Figs. 3 (a) and (b) show the total QEDCS cross section, polarized and unpolarized, respectively, as a function of the incident lepton energy E_l . We have imposed the constraints in the second column of Table I on the energies and angles of the outgoing particles, as well as those on \hat{s} . Both polarized and unpolarized cross sections increase sharply with E_l , reach a peak at around $E_l = 20$ GeV and then start to decrease. The cross section in the inelastic channel is also shown, which have similar trends except that the peak in the polarized case is broader.

A. HERMES

Figs. 4(a) and (b) show the total (elastic+inelastic) polarized and unpolarized QED Compton scattering cross sections, respectively, in bins of x_γ for HERMES kinematics, subject to the cuts of Table I. We have taken the incident electron energy $E_e = 27.5$ GeV. We also show the cross section calculated in the EPA. The same in the inelastic channel is also shown. The cross section, integrated over x_γ , agrees with the EPA within 7.1% (unpolarized) and 4.8% (polarized). From the figures it is also clear that the agreement in the inelastic channel is much better than for HERA kinematics [5, 6] (2.5% in the polarized case). This is because at HERMES Q^2 can never become too large (maximum 13.7 GeV 2), subject to our kinematical cuts, which is expected in a fixed target experiment. The agreement is not so good without the constraint $\hat{s} > 1$ GeV 2 . Fig. 4(c) shows the asymmetry, which is defined as

$$A_{LL} = \frac{\sigma_{++} - \sigma_{+-}}{\sigma_{++} + \sigma_{+-}} \quad (5.1)$$

where + and - denote the helicities of the incoming electron and proton. They are calculated with the same set of constraints. The asymmetry is quite sizable at HERMES and increases

in higher x_γ bins. The asymmetry in the EPA is also shown. It is interesting to note that the discrepancy in the cross sections with the EPA approximated estimate, actually gets canceled in the asymmetry, as a result it shows an excellent agreement with the EPA, except in the last bin. We have also shown the expected statistical error in the bins, which have been calculated using the formula, valid when the asymmetry is not too large:

$$\delta A_{LL} \approx \frac{1}{\mathcal{P}_e \mathcal{P}_p \sqrt{\mathcal{L} \sigma_{\text{bin}}}}; \quad (5.2)$$

where \mathcal{P}_e and \mathcal{P}_p are the polarizations of the incident lepton and proton, respectively, \mathcal{L} is the integrated luminosity and σ_{bin} is the unpolarized cross section in the corresponding x_γ bin. We have taken $\mathcal{P}_e = \mathcal{P}_p = 0.7$ and $\mathcal{L} = 1 \text{ fb}^{-1}$ for HERMES. The expected statistical error increases in higher x_γ bins, because the number of events become smaller. However the asymmetry seems to be measurable at HERMES.

The background from virtual Compton scattering is reduced at HERA by the experimental condition of no observable hadronic activity at the detectors. Basically the electron and photon are detected in the backward detectors and the hadronic system in the forward detectors. In our previous work, we have observed that for unpolarized scattering at HERA, such a constraint is insufficient to remove the VCS contribution for higher x_γ . We have proposed a new constraint $\hat{S} \geq \hat{s}$, where \hat{S} and \hat{s} can be measured experimentally, to be imposed on the cross section. Here, we investigate the effect of this constraint on the polarized cross section. To estimate the inelastic contribution coming from VCS, we use Eq. (4.5), together with an effective model for the parton distribution of the proton. The effective parton distribution is of the form

$$\Delta \tilde{q}(x_B, Q^2) = \Delta q(\bar{x}, Q^2 + Q_0^2), \quad (5.3)$$

$\Delta q(x_B, Q^2)$ being the NLO GRSV00 (standard scenario) distribution function [25]. In the relevant kinematical region, Q^2 can be very small and may become close to zero, where the parton picture is not applicable. The parameter $Q_0^2 = 2.3 \text{ GeV}^2$ prevents the scale of the parton distribution to become too small. \bar{x} is a suitably defined scaling variable, $\bar{x} = \frac{x_B(Q^2 + Q_0^2)}{Q^2 + x_B Q_0^2}$.

To estimate the unpolarized background effect, we use the same expressions as in [6] with an effective parton distribution given in Eq. (22) of [6]. Fig. 4(d) shows the polarized cross section in the inelastic channel at HERMES, subject to the constraints of Table I, in bins of

$\hat{s} - \hat{S}$ calculated in the 'effective' parton model. The VCS and the interference contributions are also shown. QEDCS cross sections using the Badelek *et. al* parametrization of $g_1(x_B, Q^2)$ are also plotted. In fact, the cross section in the 'effective' parton model lies close to this. Within the parton model, VCS is suppressed when $\hat{s} < \hat{S}$, similar to the unpolarized case at HERA [6]. Unlike HERA, the interference between QEDCS and VCS is not negligible at HERMES, although smaller than QEDCS in the relevant region. Since the interference term changes sign when a positron beam is used instead of the electron beam, a combination of electron and positron scattering data can eliminate this contribution. In order to estimate the VCS in the elastic channel, one needs a suitable model for the polarized generalized parton distributions. However, in the simplified approximation of a pointlike proton with an effective vertex as described in section IV, the elastic VCS as well as the interference contribution is much suppressed at HERMES. Similar observations hold for unpolarized scattering.

Fig. 5 shows the asymmetries in the inelastic channel in bins of x_B . In addition to the cuts mentioned above and shown in table I, we have also chosen $\hat{S} - \hat{s} > 2 \text{ GeV}^2$ to suppress the background. The asymmetry is small but sizable and could be a tool to access $g_1(x_B, Q^2)$ at HERMES. In fact, QED Compton events can be observed at HERMES in the kinematical region $x_B = 0.02 - 0.7$ and $Q^2 = 0.007 - 7 \text{ GeV}^2$ (small Q^2 , medium x_B). However, from the figure it is seen that the asymmetry is very small for x_B below 0.1. We have also shown the expected statistical error in each bin. The average Q^2 value in GeV^2 for the polarized cross section for each bin is shown, which has been calculated using the formula

$$\langle Q^2 \rangle = \frac{\int_{\text{bin}} Q^2 d\Delta\sigma}{\int_{\text{bin}} d\Delta\sigma} \quad (5.4)$$

B. COMPASS

Figs. 6 (a) and (b) show the cross sections in bins of x_γ for the polarized and unpolarized QEDCS for the kinematics of COMPASS. We take the energy of the incident muon beam to be 160 GeV, the target is a proton. The final muon and the photon are detected in the polar angle region $0.04 < \theta_\mu, \theta_\gamma < 0.18$. The cross sections in bins, subject to the kinematical constraints shown in Table I, are much smaller than at HERMES, because they start to decrease with the increase of the incident lepton energy E_l as E_l becomes greater than about 20 GeV, as observed in Fig. 3. As before, the cuts remove the initial and final

state radiative events. The x_γ integrated cross section agrees with the EPA within 14.2% (unpolarized) and 15.5% (polarized). The agreement thus is not as good as at HERMES. From the figures it is seen that the cross section in the EPA actually lies below the 'exact' one, both for polarized and unpolarized cases. This discrepancy is due to the fact that the EPA is expected to be a good approximation when the virtuality of the exchanged photon is small. At COMPASS, with our kinematical cuts, Q^2 can not reach a value below 0.07 GeV² and can be as large as 144 GeV², whereas for HERMES smaller values of Q^2 are accessible (see the previous subsection). Fig. 6(c) shows the asymmetry in bins of x_γ , the asymmetry in the inelastic channel is also shown. The asymmetry is of the same order of magnitude as in HERMES and is in good agreement with the EPA. We have also shown the expected statistical error in each bin, calculated using Eq. (5.2). We have taken $\mathcal{P}_e = \mathcal{P}_p = 0.7$ and $\mathcal{L} = 1fb^{-1}$ for COMPASS. The statistical error is large in higher x_γ bins. Fig. 6(d) shows the polarized QEDCS, VCS and interference contributions (inelastic) calculated in the 'effective' parton model, in bins of $\hat{s} - \hat{S}$. As in HERMES, VCS is suppressed for $\hat{s} < \hat{S}$. The interference term is not suppressed but using μ^+ and μ^- beams this can be eliminated. We have also plotted the QEDCS cross section using Badelek *et al.* parametrization of $g_1(x_B, Q^2)$. The VCS and the interference contributions (elastic) are much suppressed in the pointlike approximation of the proton with the effective vertex. Fig. 7 shows the asymmetry at COMPASS in the inelastic channel plotted in bins of x_B with the same set of constraints and the additional cut $\hat{S} - \hat{s} > 2$ GeV². The asymmetry is sizable and can give access to $g_1(x_B, Q^2)$, the kinematically allowed range is $0.07 < x_B < 0.2$. We have also shown the expected statistical errors in the bins and the average Q^2 in each bin. Comparing Fig. 5 and 7 one can see that there is no overlap in the kinematical region covered at HERMES and COMPASS. Higher values of Q^2 are probed at COMPASS in the same x_B range as compared to HERMES.

C. eRHIC

The cross sections for eRHIC kinematics, both polarized and unpolarized, are shown in Fig. 8(a) and (b), respectively, in bins of x_γ . We have taken the incident electron energy $E_e = 10$ GeV and the incident proton energy $E_p = 250$ GeV. The cross section in the EPA is also shown. The kinematic constraints are given in Table I. The polar angle acceptance of

the detectors at eRHIC is not known. We have taken the range of θ_e, θ_γ to be the same as at HERA. We have checked that the constraints on the energies and the polar angles of the outgoing electron and photon are sufficient to prevent the electron propagators to become too small and thus reduce the radiative contributions. The unpolarized total (elastic+inelastic) cross section, integrated over x_γ agrees with the EPA within 1.6%. The agreement in the inelastic channel is about 6.3%. The polarized total cross section agrees with the EPA within 9.8%. The EPA in this case lies below the 'exact' one in all the bins. The agreement in the inelastic channel is about 19.6%. More restrictive constraints instead of $\hat{s} > Q^2$, like $\hat{s} > 10 Q^2$, makes the agreement better, about 1.2% in the polarized case and 1.9% in the unpolarized case. Fig. 8(c) shows the asymmetry for eRHIC, in bins of x_γ . The discrepancy in the cross section cancels in the asymmetry, as a result good agreement with the EPA is observed in all bins except the last one at higher x_γ . The asymmetry in the inelastic channel is also shown. We have plotted the expected statistical error in the bins using Eq. (5.2). For eRHIC, we have taken $\mathcal{P}_e = \mathcal{P}_p = 0.7$ and $\mathcal{L} = 1fb^{-1}$. The expected statistical error increases in higher x_γ bins. The asymmetry is very small for small x_γ but becomes sizable as x_γ increases. Fig. 8(d) shows the polarized cross section in the inelastic channel, in bins of $\hat{s} - \hat{S}$, in the 'effective' parton model for eRHIC. The VCS is suppressed in all bins, especially for $\hat{s} < \hat{S}$. The interference contribution is negligible, similar to HERA. The 'effective' parton model QEDCS cross section is also compared with the more exact one, using Badelek *et. al.* parametrization for $g_1(x_B, Q^2)$. Similar effects are observed in the unpolarized case. In the pointlike approximation of the proton with the effective vertex, as before, the elastic VCS as well as the interference contributions are very much suppressed. Fig. 9 shows the asymmetry in bins of x_B in the inelastic channel, which may be relevant for the determination of $g_1(x_B, Q^2)$ using QEDCS at eRHIC. The asymmetry is small but sizable, however the error bars are large and therefore good statistics is needed. x_B can be as low as 0.002. A wide range of Q^2 can be accessed at eRHIC starting from 0.008 to 2000 GeV²; the average Q^2 value in the bins ranges from 2.4 to 315 GeV². Fig. 10 shows the total asymmetry in Q^2 bins for eRHIC. The asymmetry in this case is bigger in each bin and the error bars are smaller than the x_B bins except the last bin for high Q^2 where the number of events are smaller.

VI. SUMMARY AND CONCLUSIONS

To summarize, in this paper we have analyzed the QED Compton process in polarized lp scattering, both in the elastic and inelastic channel. This process has a distinctive experimental signature and we showed that the cross section can be expressed in terms of the equivalent photon distribution of the polarized proton, convoluted with the real photoproduction cross section. The EPA is a useful tool to estimate high energy scattering cross sections; however the accuracy of this approximation and the kinematical region of its validity have to be checked by experiment. In this work we provided the necessary kinematical constraints for the extraction of the polarized photon content of the proton by measuring the QED Compton process at HERMES, COMPASS and eRHIC. We showed that the cross section and, in particular, the asymmetries are quite accurately described by the EPA. We also discussed the possibility of suppressing the major background process, namely the virtual Compton scattering. We pointed out that such an experiment can give access to the spin structure function $g_1(x_B, Q^2)$ in the region of low Q^2 and medium x_B in fixed target experiments and over a broad range of x_B , Q^2 at the future polarized ep collider, eRHIC. Because of the different kinematics compared to the fully inclusive processes, the QED Compton process can provide information on $g_1(x_B, Q^2)$ in a range not well-covered by inclusive measurements and thus is a valuable tool to have a complete understanding of the spin structure function.

VII. ACKNOWLEDGEMENTS

We warmly acknowledge E. Reya and M. Glück for initiating this study, as well as for many fruitful discussions. We also thank W. Vogelsang for helpful discussions and suggestions. This work has been supported in part by the 'Bundesministerium für Bildung und Forschung', Berlin/Bonn.

APPENDIX A: MATRIX ELEMENT FOR THE ELASTIC BACKGROUND VIRTUAL COMPTON SCATTERING PROCESS

The explicit expressions of the matrix elements in section IV are given below:

$$|\Delta M_{\text{el}}^{QEDCS}|^2 = \frac{4}{t \hat{s} \hat{u}} \left[-A + \frac{2m^2}{t S'} B \right] F_1^2(t), \quad (\text{A1})$$

$$|\Delta M_{\text{el}}^{VCS}|^2 = -\frac{4}{\hat{t} U' \hat{S}'} \left[A + \frac{2m^2}{\hat{S}' S' U'} C \right] F_1^2(\hat{t}), \quad (\text{A2})$$

with

$$A = 2t^2 + (\hat{s} - 2S' - \hat{u})(\hat{s} + \hat{u}) - 2t(\hat{s} - 2S' - U') - 2\hat{u}U', \quad (\text{A3})$$

$$B = -2t^3 + \hat{s}^3 - \hat{s}\hat{u}^2 + 2t^2(2\hat{s} + \hat{u}) - t(3\hat{s}^2 + \hat{u}^2), \quad (\text{A4})$$

$$\begin{aligned} C = & (\hat{s} + \hat{u})^2 [-2S'^2 + \hat{s}\hat{u} - 2S'\hat{u} - \hat{u}^2 + 2m^2(\hat{s} + \hat{u} - t) - t(S' + \hat{u})] \\ & - (\hat{s} + \hat{u}) [2t^2 - 3t\hat{s} + \hat{s}^2 + \hat{s}(S' - 2\hat{u}) + 3\hat{u}(S' + \hat{u})] U' \\ & - [2t^2 + s^2 - \hat{s}\hat{u} + 2\hat{u}^2 - t(3\hat{s} + \hat{u})] U'^2. \end{aligned} \quad (\text{A5})$$

$$2 \Re e \Delta M_{\text{el}}^{QEDCS} \Delta M_{\text{el}}^{VCS*} = -\frac{4}{t \hat{s} \hat{u} \hat{t} U' \hat{S}'} \left[D + \frac{2m^2 E}{S'} \right] F_1(\hat{t}) F_1(t), \quad (\text{A6})$$

where D and E read:

$$\begin{aligned} D = & [2t^2 + (\hat{s} - 2S' - \hat{u})(\hat{s} + \hat{u}) - 2t(\hat{s} - 2S' - U') - 2\hat{u}U'] \\ & \times \{(\hat{s} + \hat{u})[\hat{t}\hat{u} + S'(\hat{s} + \hat{u})] + [t(\hat{s} - \hat{u}) + \hat{s}(\hat{s} + \hat{u})]U'\}, \end{aligned} \quad (\text{A7})$$

$$\begin{aligned} E = & [\hat{s}(\hat{s} - t)^2(\hat{s} - 2t) + (2t^3 - t^2\hat{s} - \hat{s}^3)\hat{u} + (-2t^2 - 3t\hat{s} + \hat{s}^2)\hat{u}^2 + (t + 3\hat{s})\hat{u}^3] U' \\ & - (\hat{s} + \hat{u}) \{ -2t^3\hat{u} - (\hat{s} + \hat{u})[\hat{s}^2(S' - 2\hat{u}) + S'\hat{u}^2 + 2\hat{s}\hat{u}(S' + \hat{u})] \\ & - t[-7\hat{s}S'\hat{u} + \hat{u}^2(-2S' + \hat{u}) + \hat{s}^2(-3S' + 5\hat{u})] + t^2[2\hat{u}(\hat{u} - S') + \hat{s}(5\hat{u} - 2S')] \}. \end{aligned} \quad (\text{A8})$$

We have introduced the invariants $U = (P - k')^2$, $\hat{u} = (l - k')^2$ and $\hat{S} = -(\hat{s} + \hat{u} + U' - m^2)$ and used the notations $S' = S - m^2$, $U' = U - m^2$, $\hat{S}' = \hat{S} - m^2$ for compactness.

APPENDIX B: MATRIX ELEMENT FOR THE INELASTIC VIRTUAL COMPTON SCATTERING BACKGROUND PROCESS

For the corresponding inelastic channel in section IV the explicit matrix elements are given by:

$$|\Delta M_{\text{inel}}^{QEDCS}|^2 = 4 e_q^2 \frac{F}{Q^2 \hat{s} \hat{u}}. \quad (\text{B1})$$

$$|\Delta M_{\text{inel}}^{VCS}|^2 = -4 e_q^4 \frac{F}{\hat{t} \hat{S} \hat{U}}, \quad (\text{B2})$$

with $\hat{S} = -(\hat{s} + \hat{u} + x_B U')$, $\hat{U} = x_B U'$ and

$$F = \hat{s}^2 - \hat{u}^2 + 2Q^4 + 2Q^2 \hat{s} - 2x_B [\hat{s}S' + \hat{u}(S' + U') + Q^2(2S' + U')]. \quad (\text{B3})$$

Here e_q is the charge of the parton in units of the proton charge. Finally

$$2 \Re e \Delta M_{\text{inel}}^{QEDCS} \Delta M_{\text{inel}}^{VCS*} = -4 e_q^3 \frac{G H}{Q^2 \hat{s} \hat{u} \hat{t} \hat{S} \hat{U}}, \quad (\text{B4})$$

with

$$G = 2Q^4 + \hat{s}^2 - 2\hat{s}S'x_B - \hat{u}[\hat{u} + 2(S' + U')x_B] + 2Q^2[\hat{s} - (2S' + U')x_B] \quad (\text{B5})$$

$$H = Q^2[\hat{s}(\hat{u} - \hat{U}) + \hat{u}(\hat{u} + \hat{U})] - x_B (\hat{s} + \hat{u})[S' \hat{u} + \hat{s}(S' + U')] \quad (\text{B6})$$

- [1] J. Blümlein, G. Levman, H. Spiesberger, J. Phys. **G 19**, 1695 (1993).
- [2] A. De Rujula, W. Vogelsang, Phys. Lett. **B 451** 437 (1999).
- [3] A. Courau and P. Kessler, Phys. Rev. **D 46**, 117, (1992).
- [4] V. Lendermann, H. C. Schultz-Coulon, D. Wegener, Eur. Phys. J. **C 31** 343 (2003).
- [5] A. Mukherjee, C. Pisano, Eur. Phys. J. **C 30**, 477 (2003).
- [6] A. Mukherjee, C. Pisano, hep-ph/0402046, to appear in Eur. Phys. J. C.
- [7] M. Glück, C. Pisano, E. Reya, Phys. Lett. **B 540**, 75, (2002).
- [8] M. Glück, C. Pisano, E. Reya, I. Schienbein, Eur. Phys. J. **C 27**, 427 (2003).
- [9] K. Abe *et. al.*, Phys. Rev. **D 58**, 112003 (1998).

- [10] A. Airapetian *et. al.*, Phys. Lett. **B 494**, 1 (2000).
- [11] A. Airapetian *et. al.*, Phys. Rev. Lett. **B 90**, 092002, (2003).
- [12] M. Amarian *et. al.*, Phys. Rev. Lett. **89**, 242301 (2002).
- [13] J. Yun *et. al.*, Phys. Rev. **C 67**, 055204, (2003).
- [14] R. Fatemi *et. al.*, Phys. Rev. Lett. **91**, 222002, (2003).
- [15] B. Badelek, Acta Phys. Pol. **B 34**, 2943 (2003)
- [16] B. Lampe and E. Reya, Phys. Rept. **332**, 1 (2000).
- [17] S. D. Bass and A. De Roeck, Nucl. Phys. B (Proc. Suppl.) **105**, 1 (2002)
- [18] B. Kniehl, Phys. Lett. **B 254**, 267, (1991).
- [19] D. de Florian, S. Frixione, Phys. Lett. **B 457**, 236, (1999).
- [20] X. Ji, Phys. Rev. **D 55**, 7114 (1997).
- [21] For reviews on generalized parton distributions, see M. Diehl, Phys. Rept., **388**, 41 (2003); X. Ji, J. Phys. **G 24**, 1181 (1998); A. V. Radyushkin, hep-ph/0101225, published in "At the Frontier of Particle Physics/Handbook of QCD", ed. M. Shifman (World Scientific, Singapore, 2001); K. Goeke, M. V. Polyakov, M. Vanderhaeghen, Prog. Part. Nucl. Phys. **47**, 401 (2001).
- [22] V. Lenderman, Ph. D. thesis, Univ. Dortmund, H1 collaboration, DESY-THESIS-2002-004, (2002).
- [23] H. Abramowicz and A. Levy, hep-ph/9712415; corrected according to a private communication by the authors.
- [24] B. Badelek, J. Kwiecinski and B. Ziaja, Eur. Phys. J. **C 26**, 45 (2002).
- [25] M. Glück, E. Reya, M. Stratmann and W. Vogelsang, Phys. Rev. **D 63**, 094005 (2001).

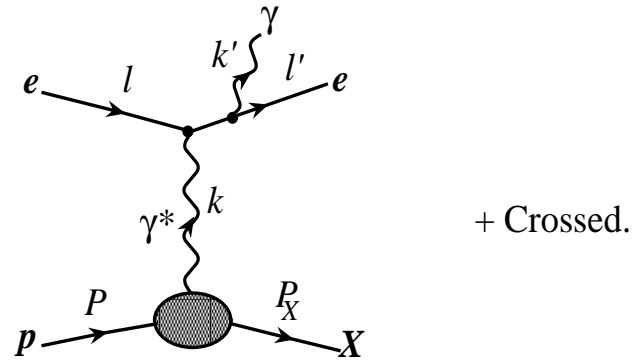


Fig. 1: Feynman diagrams for the QED Compton process (QEDCS). $X \equiv p$ (and $P_X \equiv P'$) corresponds to elastic scattering.

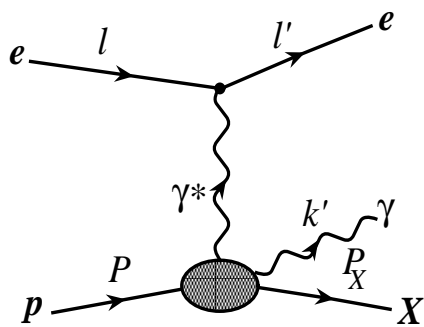


Fig. 2: As in Fig. 1 but for the virtual Compton scattering (VCS) background process.

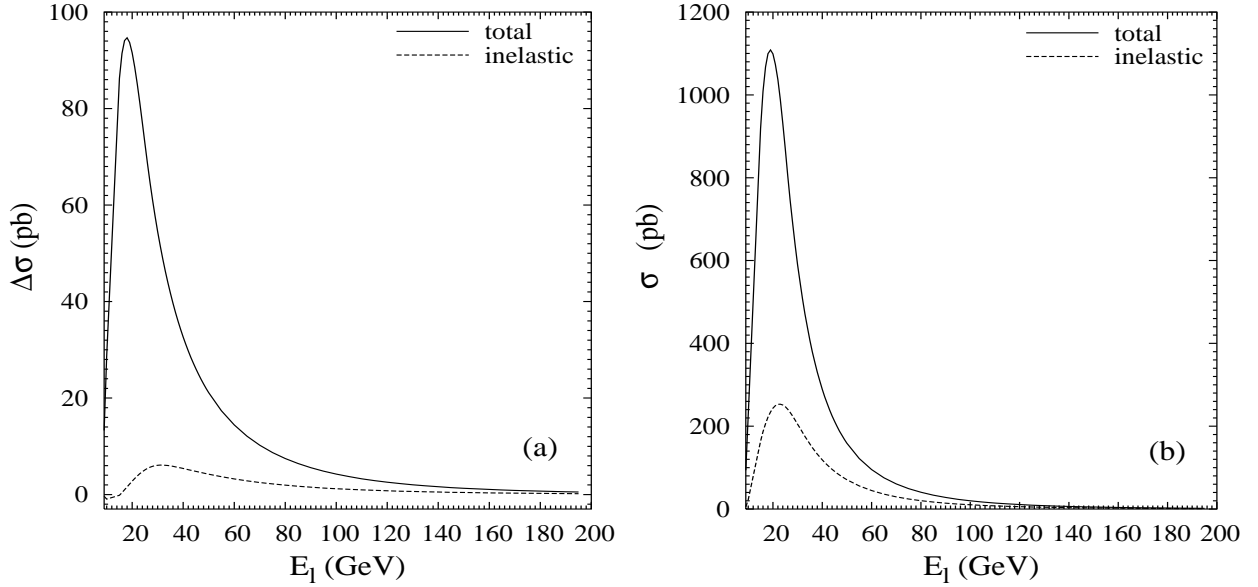


Fig. 3: QEDCS cross section vs. energy of the incident lepton; (a) polarized, (b) unpolarized.

The continuous line is the total cross section and the dashed line is the cross section in the inelastic channel. The cuts imposed are given in the central column of table I. We have used the ALLM paramtrization of F_2 [23] and the Badelek *et. al* parametrization of g_1 [24].

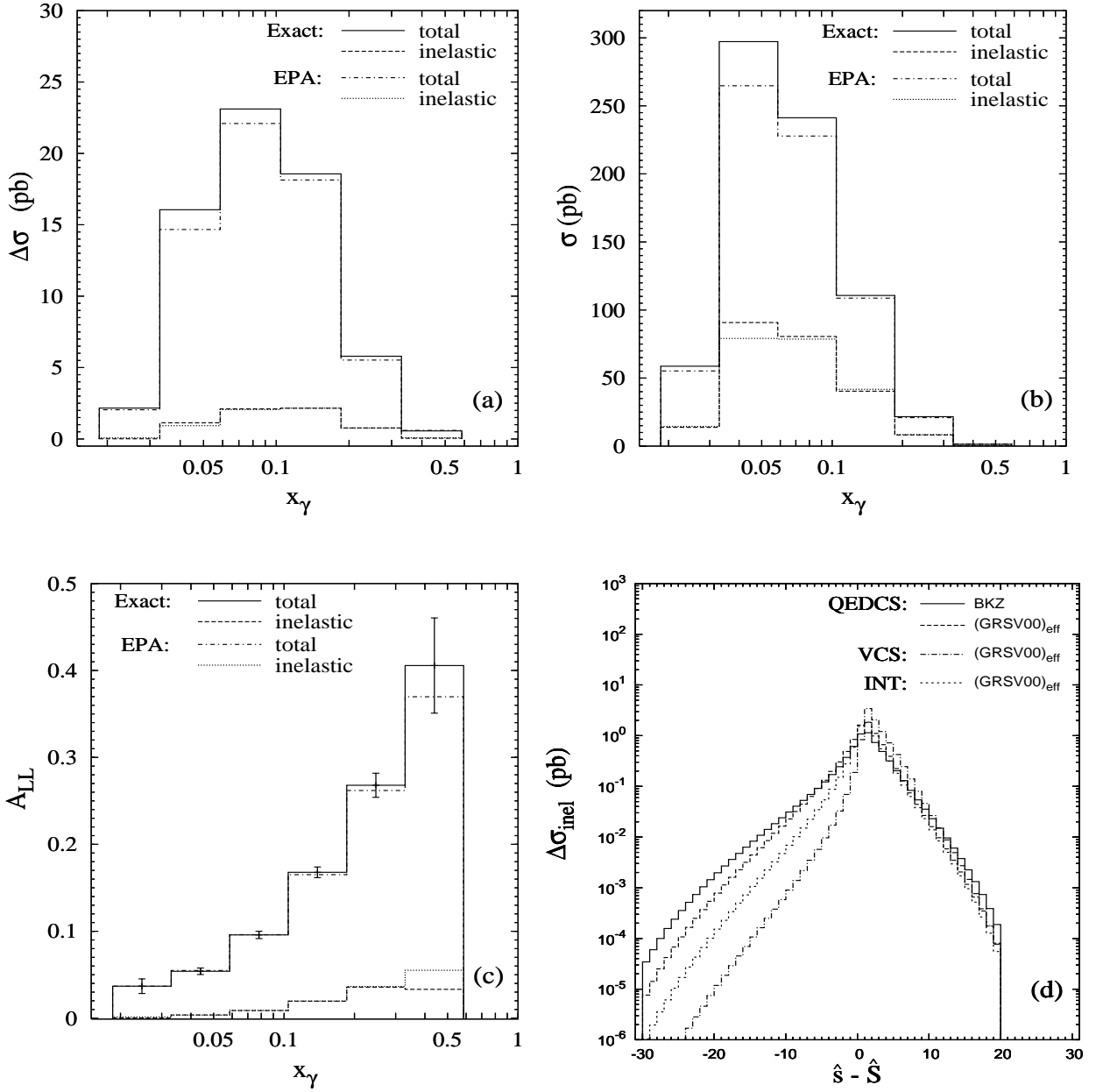


Fig. 4: Cross section for QED Compton scattering (QEDCS) at HERMES in bins of x_γ (a) polarized, (b) unpolarized, (c) the asymmetry; for the polarized cross section Badelek *et al.* [24] parametrization of g_1 (BKZ) and for the unpolarized cross section ALLM parametrization of F_2 have been used; (d) polarized inelastic cross section for QEDCS (long dashed), VCS (dashed-dotted) and the interference (dashed) at HERMES in the effective parton model. The bins are in $\hat{s} - \hat{S}$, expressed in GeV^2 . The continuous line is the QEDCS cross section using the BKZ parametrization of $g_1(x_B, Q^2)$. The constraints imposed are given in Table I.

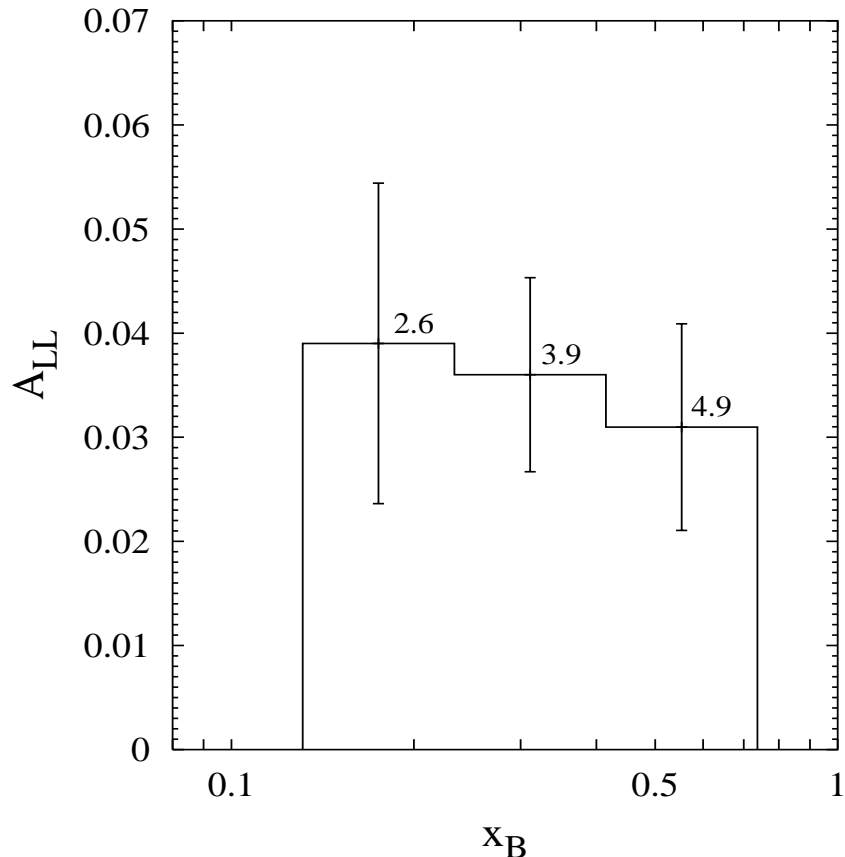


Fig. 5: Asymmetry in the inelastic channel in bins of x_B at HERMES. We have used Badelek *et al.* [24] parametrization of g_1 . The constraints imposed are as in Table I (except $\hat{s} > Q^2$), together with $\hat{S} - \hat{s} > 2$ GeV 2 . The average Q^2 (in GeV 2) of each bin is also shown.

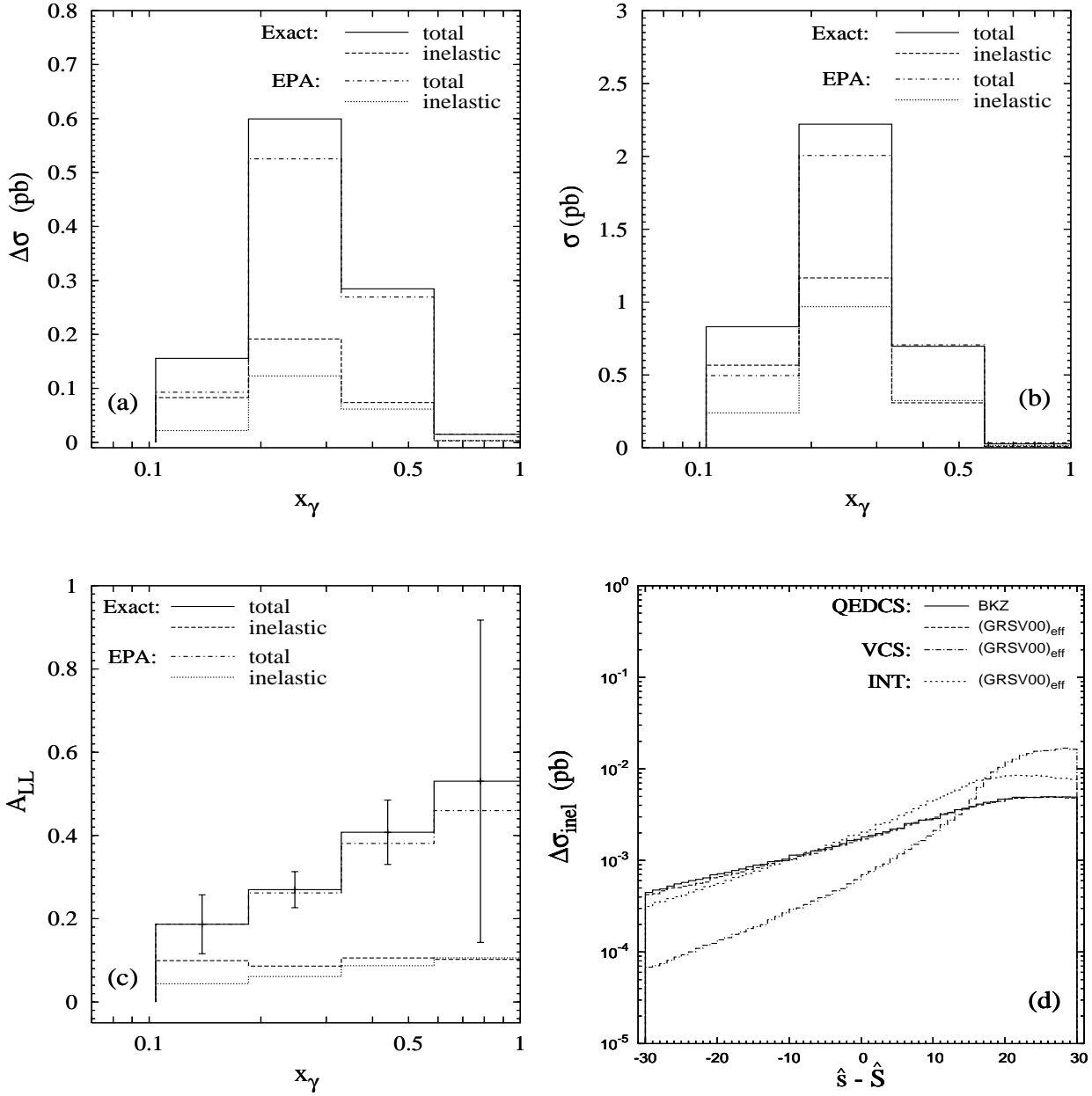


Fig. 6: (a), (b), (c) and (d) are the same as in Fig. 4 but for COMPASS. The constraints imposed are given in Table I.

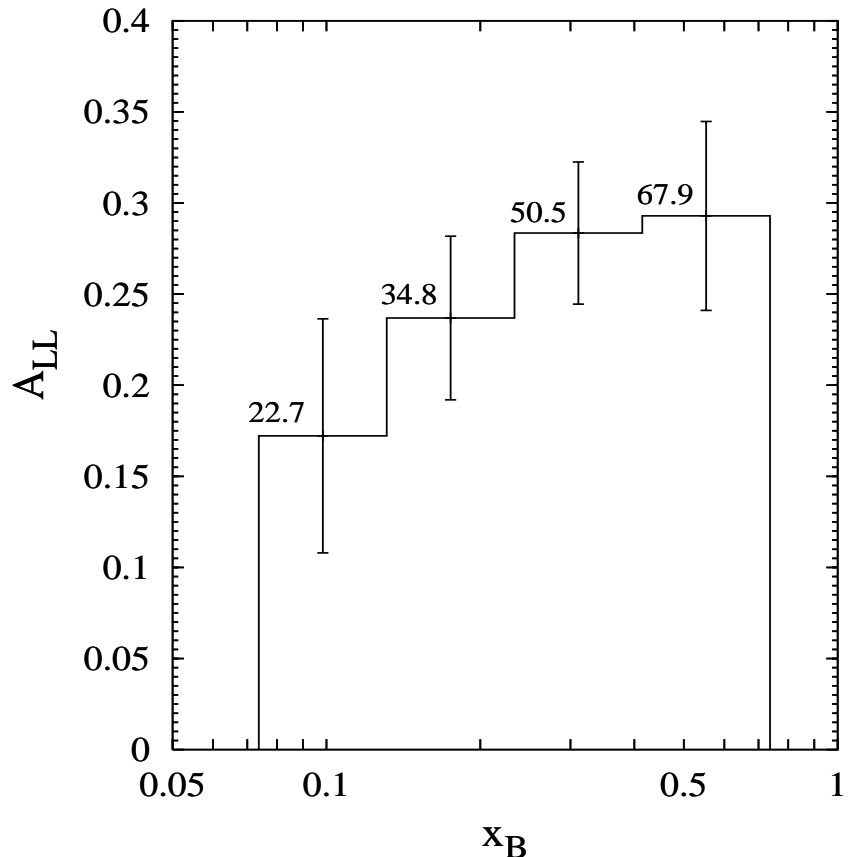


Fig. 7: Asymmetry in the inelastic channel in bins of x_B at COMPASS. We have used Badelek *et al.* [24] parametrization of g_1 . The constraints imposed are as in Table I (except $\hat{s} > Q^2$), together with $\hat{S} - \hat{s} > 2$ GeV 2 . The average Q^2 (in GeV 2) of each bin is also shown.

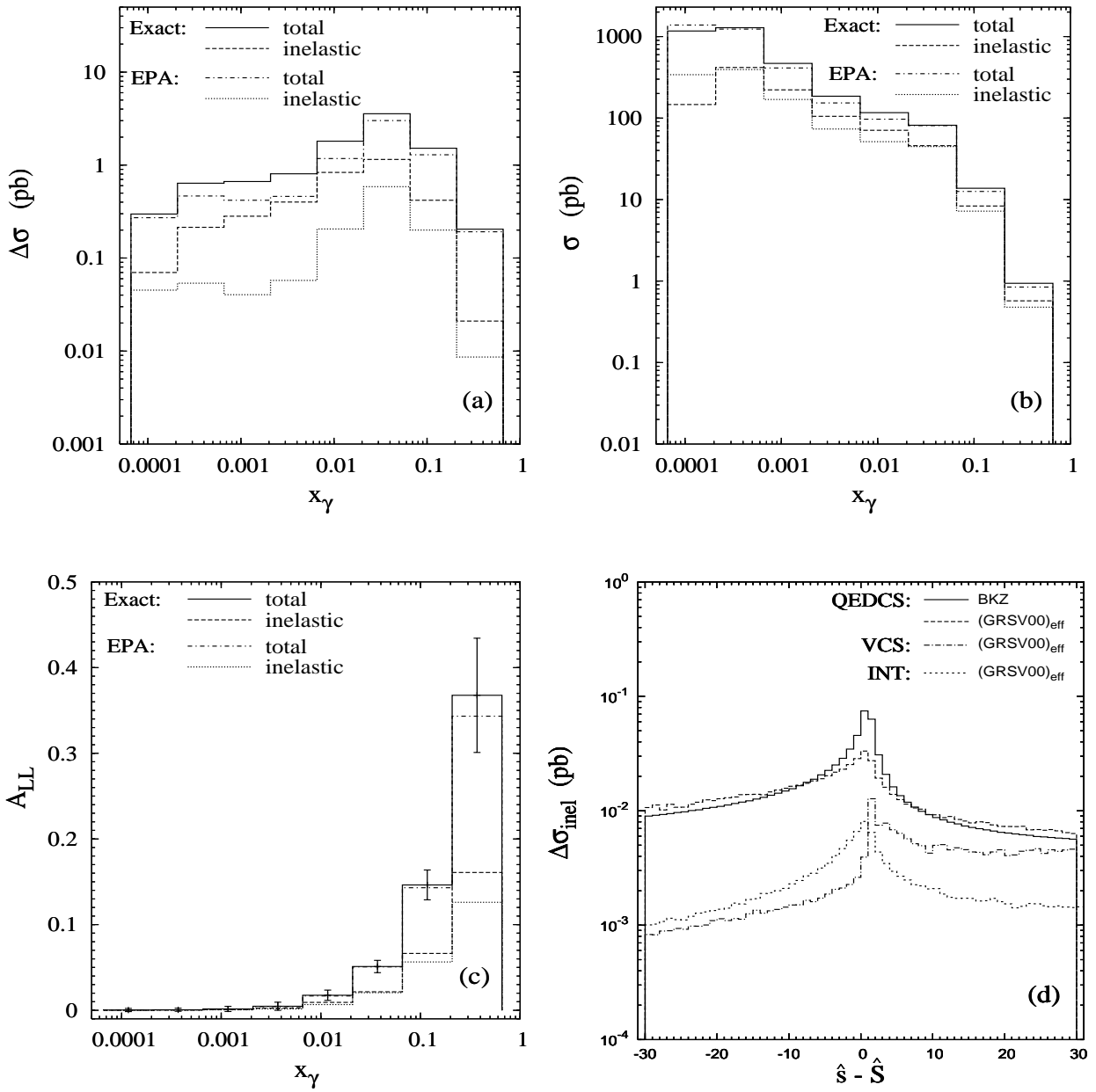


Fig. 8: (a), (b), (c) and (d) are the same as in Fig. 4 but for eRHIC. The constraints imposed are given in Table I.

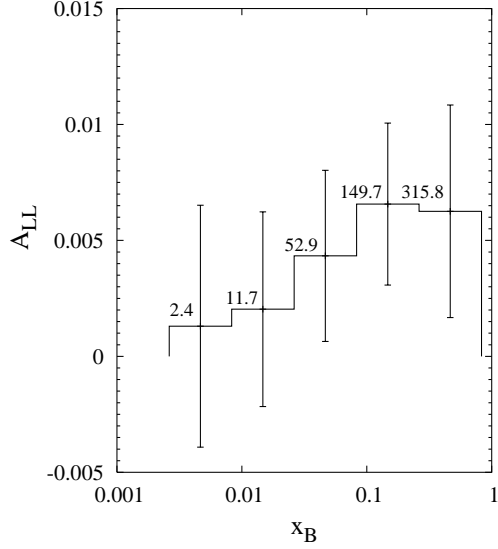


Fig. 9: Asymmetry in the inelastic channel in bins of x_B at eRHIC. We have used Badelek *et al.* [24] parametrization of g_1 . The constraints imposed are as in Table I (except $\hat{s} > Q^2$), together with $\hat{S} > \hat{s}$. The average Q^2 (in GeV 2) of each bin is also shown.

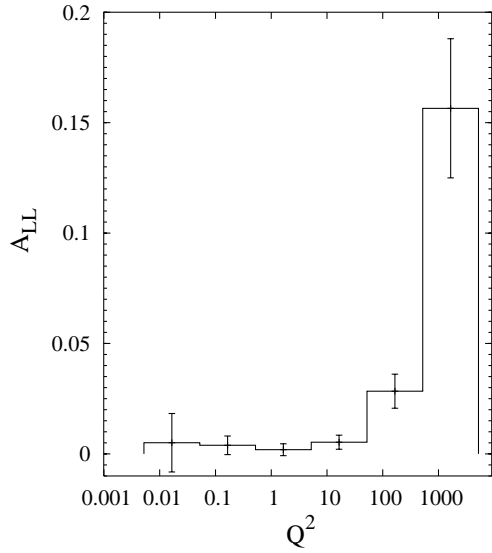


Fig. 10: Asymmetry in bins of Q^2 (GeV 2) at eRHIC. We have used Badelek *et al.* [24] parametrization of g_1 . The constraints imposed are the same as in Fig. 9.

HERMES	COMPASS	eRHIC
$E_e = 27.5 \text{ GeV}$ $0.04 < \theta_e, \theta_\gamma < 0.2$ $E'_e, E'_\gamma > 4 \text{ GeV}$ $\hat{s} > 1 \text{ GeV}^2$ $\hat{s} > Q^2$	$E_\mu = 160 \text{ GeV}$ $0.04 < \theta_\mu, \theta_\gamma < 0.18$ $E'_\mu, E'_\gamma > 4 \text{ GeV}$ $\hat{s} > 1 \text{ GeV}^2$ $\hat{s} > Q^2$	$E_p = 250 \text{ GeV}$ $E_e = 10 \text{ GeV}$ $0.06 < \theta_e, \theta_\gamma < \pi - 0.06$ $E'_e, E'_\gamma > 4 \text{ GeV}$ $\hat{s} > 1 \text{ GeV}^2$ $\hat{s} > Q^2$

TABLE I: Energies, angular acceptance and kinematical cuts for various experiments.